Energy Equip. Sys./ Vol. 10/No. 4/Dec. 2022/ 389-399

ENERGY EQUIPSYS

Energy Equipment and Systems

http://energyequipsys.ut.ac.ir
www.energyequipsys.com

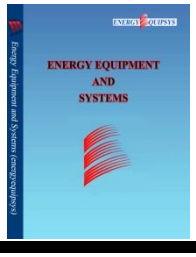

Effect of grid resolution on NACA0012 self-noise prediction by large eddy simulation

Authors

Seyed Mohammad Hasheminasab[a]
Seyed Mohammad Hossein Karimian[a*]
Sahar Noori[a]

[a] Department of Aerospace Engineering, Amirkabir University of Technology, No. 350, Hafez Ave, Tehran 159163-4311, Iran

Article history:

Received : 27 October 2021
Accepted : 2 January 2022

ABSTRACT

Airfoil self-noise is one of the dominant sources of airframe noises which causes limitations in many applications such as wind turbines. This paper investigates and quantifies the sensitivity of airfoil self-noise prediction to the grid resolution using large eddy simulation. Three-dimensional incompressible fluid flow around a NACA0012 airfoil at zero angle of attack with a chord-based Reynolds number of 6.4×10^5 is numerically analyzed in this paper. Far-field noise is predicted by Ffowcs-Williams & Hawkings model using the results of large eddy simulation. Three different grid sizes are used to investigate the effect of grid resolution on the accuracy of self-noise prediction. Results are compared with the experimental data of wind tunnel tests and noise measurements with microphones. Although the aerodynamic properties are calculated accurately in all grids, the grid resolution over the surface has a significant effect on the accuracy of the noise prediction. This effect of grid resolution is quantified in this paper. By the increase of grid points in the spanwise and streamwise directions on the surface, numerical noise prediction has approached the experimental data. The difference with the experimental data decreases from 20 dB to 3 dB in some frequencies. In addition, having doubled the number of surface grid points in both directions the average percentage of difference with the experimental data decreases from 5% to 2%.

Keywords: Large-Eddy Simulation, Grid Resolution, Aeroacoustics, Self-Noise.

1. Introduction

Aerodynamic noise has received growing attention from the public over the past few decades. The dominant source of this is the trailing-edge noise which is generated by the interaction of the turbulent boundary layer and the sharp trailing edge and is referred to as Turbulent Boundary Layer-Trailing Edge (TBL-TE) noise [1]. This noise is important in many applications such as wind turbines [2], propellers [3], rotors [4].

TBL-TE noise can be predicted using empirical models as the work by De Gennaro et al. [5] and experimental approaches [6]. An alternative is using computational aeroacoustics (CAA) methods based on Lighthill's theory [7] and followed by various aeroacoustic analogies such as the one by Ffowcs Williams et al. [8] which later developed by Lilly [9]. The required

* Corresponding author: Seyed Mohammad Hossein Karimian
Department of Aerospace Engineering, Amirkabir University of Technology, No. 350, Hafez Ave, Tehran 159163-4311, Iran

input parameters for accurate noise predictions still reside in data that is best accessed from numerical simulations [10]. An accurate prediction of far-field noise requires well resolved transient flow field data, especially the flow field near the solid surfaces [11]. Depending on the computational resources available, this is best facilitated through using Direct Numerical Simulation (DNS) and/or Large Eddy Simulation (LES). Although high-fidelity computational methods can provide detailed information on noise sources, still the computational cost is a concern based on the computing facilities. Mesh resolution plays a crucial role in performing an accurate simulation with a reasonable computational cost.

More recently, a variety of large-eddy simulations were performed to generate the source terms for wave propagation equations. Wang et al. performed LES computations of the flow past an asymmetrically beveled trailing edge of a flat strut at a chord Reynolds number of $Re = 2.15 \times 10^6$ [12]. The computed mean and fluctuating velocity profiles compare reasonably well with the experimental measurements. They concluded that, in order to accurately predict noise radiation using the LES solution, the size of the spanwise domain must be larger than the coherence length of the source field in the spanwise direction. Wasala et al. [13] used Ansys Fluent (ANSYS Inc.) for LES and CAA analogies for the prediction of noise generated by the outer part of a CART-2 wind turbine blade. Results show a good agreement with experimental data. An incompressible LES was performed by Winkler [14] over a NACA 6512-63 airfoil at zero angle of attack with Reynolds number of $Re = 1.9 \times 10^5$ for near-field noise source identification. Three different CAA methods were used for far-field noise measurement and results were compared to experimental data. Wolf et al. [15] used compressible LES and the FW-H analogy to predict the airfoil trailing edge noise. The overset mesh was used in this study and the maximum values of grid spacing in terms of wall units are given by $\Delta x^+ = 60$, and $\Delta z^+ = 20$. An excellent agreement compared to the experimental data is reported. In one of the most recent studies, the effect of implementing different flow simulation methods on the predicted noise is studied by Chen et al. [16]. The results show the sensitivity of the noise prediction on the solution methods, especially in Reynolds numbers higher than $Re = 5 \times 10^5$. In addition to the effect of the solution method, the mesh resolution and quality impact on the predicted noise has always been a concern. Winkler et al. [10] investigated the effect of grid refinement in LES on the same geometry and flow conditions for trailing edge noise prediction. The results were compared with experimental and theoretical predictions for far-field noise. The comparison revealed that different boundary conditions in the LES domain led to different results, and only under carefully matched conditions to the experiments would the LES approach be comparable to that of a wind-tunnel. Lockard et al. [17] studied the grid sensitivity for slat noise simulation. The solution method is a hybrid RANS-LES and investigates the influence of the grid on unsteady high-lift simulations to gain a better understanding of the physics responsible for noise generation and radiation. Ueno et al. [18] implemented combined RANS/LES and Cartesian mesh to predict the noise of a high-lift airfoil. It's reported that the results depend on the grid density and the grid resolution has a significant effect on surface unsteadiness. Coarse grid results in both overestimation and underestimation in pressure fluctuations, but it's not necessarily more accurate to use finer grids. More recently Yin et al. [19] presented a mesh study for airfoil trailing-edge noise prediction by Reynolds-averaged Navier-Stokes equations (RANS). Three different meshes including C-type structured mesh, overset mesh, and Cartesian mesh have been studied and it's claimed that the C-type mesh has the highest accuracy of noise prediction while the overset and Cartesian meshes overpredicted and underpredicted noise levels respectively.

Despite the studies on the effect of different solution methods and mesh quality, the sensitivity of the predicted far-field noise from LES to the grid resolution is not well known and quantified. According to the high computational costs of the wall resolved LES it's of great importance to know which grid resolution is sufficient for the accurate prediction of airfoil self-noise by LES. In this

work, an incompressible large eddy simulation of flow over a NACA0012 airfoil at zero angle of attack is performed, and far-field noise is predicted using Ffowcs-Williams & Hawkings (FW-H) acoustic analogy. Three different grid resolutions are employed, and results are compared with the experimental wind tunnel data to quantify the sensitivity of the results to the grid resolution.

Nomenclature

a_0	speed of sound in air
c	chord length
C_S	Smagorinsky constant
f	frequency
L	span
M	Mach number
$\overline{p}$	filtered pressure
p'	sound pressure
r_e	observer distance
Re	Reynolds number
$\overline{S}_{ij}$	filtered strain rate tensor
St	Strouhal number
t	time
T_{ij}	Lighthill stress tensor
u_i	fluid velocity in i −direction
u_n	fluid velocity normal to the surface
$\overline{u}_i$	filtered velocity
v_i	surface velocity in i −direction
v_n	Surface velocity normal to the surface

Greek symbols

δ_{ij}	Kronecker delta
δ_p	boundary layer thickness
$\bar{\Delta}$	grid-level filter width
$\tilde{\Delta}$	test-grid-level filter width
Δt	time step size
Δx^+	normalized wall grid size in x direction
Δy^+	normalized wall grid size in y direction
Δz^+	normalized wall grid size in z direction
ν_{sgs}	SGS eddy viscosity
ρ	density
ρ_0	air density
τ_{ij}	SGS stress tensor

Acronyms

CAA	Computational aeroacoustics
CFD	Computational Fluid Dynamics
CFL	Courant-Friedrichs-Lewy
DNS	Direct Numerical Simulation
DSM	Dynamic Smagorinsky Model
FW-H	Ffowcs-Williams & Hawkings
LES	Large Eddy Simulation
NACA	National Advisory Committee for Aeronautics
RANS	Reynolds-averaged Navier–Stokes equations
SGS	Sub-grid Scale
SPL	Sound Pressure Level
TBL-TE	Turbulent Boundary Layer-Trailing Edge

2. Simulation

2.1. Geometry and grid resolution

Flow around a NACA0012 is simulated using commercial CFD code. A C-type domain with the dimensions as shown in Fig. 1 is selected for the simulation. The C-type cartesian mesh has been chosen due to the better accuracy in noise predictions[19]. The distance from the inlet to the leading edge is selected to be 12.5c and the spanwise length of the airfoil is 0.1c. The chord length of the airfoil is c = 0.3048 m which is selected to be the same as the experimental acoustic tests of NASA report[6]. The Reynolds number based on the chord length is $Re = 6.4\times10^5$.

Constant velocity inlet is selected for the inlet boundary condition where the total pressure is not fixed but will rise (in response to the computed static pressure) to whatever value is necessary to provide the prescribed velocity distribution. A velocity magnitude of 31.7 m/s in the x-direction and the turbulent intensity of 5% and the turbulent viscosity ratio of 10 is prescribed on the inlet boundary. The pressure outlet which fixes static pressure to the specified value on outlet boundaries are used as boundary conditions and the gauge pressure at the outlet is set to zero. The boundary condition on the airfoil surface is specified as a stationary wall with the no-slip condition. Symmetry condition is prescribed on side surfaces. There is no convective flux across the symmetry plane, the normal velocity component at the symmetry plane is thus zero. Also, since there is no diffusion flux across the symmetry plane, the normal gradients of all flow variables are zero.

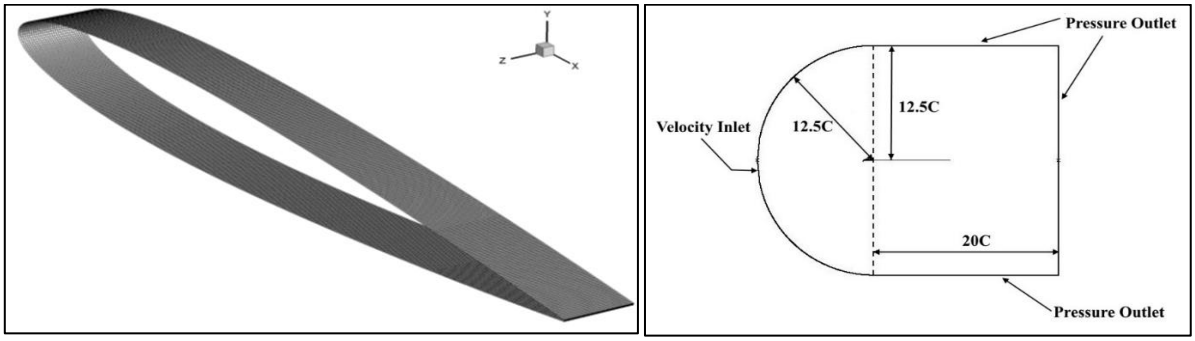

Fig. 1. Geometry, computational domain size, and boundary conditions.

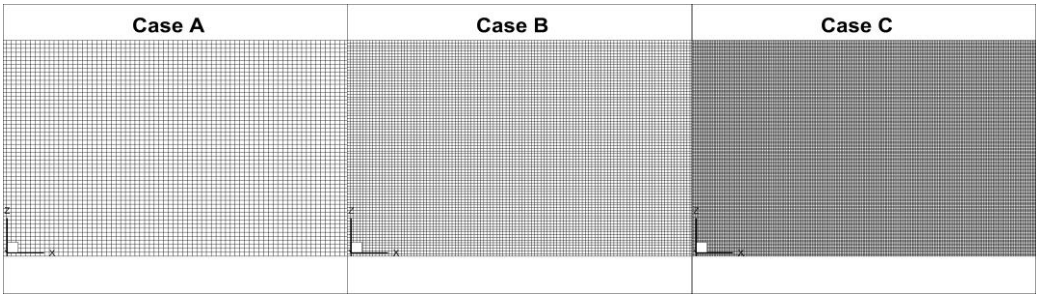

Fig. 2. Grid resolution of three studied cases

Table 1. Summery of grids' parameters

Case	A	B	C
	Low Res.	Medium Res.	High Res.
total no. of cells	2.7×10^6	8.1×10^6	21.4×10^6
Max Δz^+(Δx^+)	75	50	25
number of nodes in z-direction	53	80	160
Max Δy^+	1.2	1	1

As shown in Fig. 2 three different grids are developed to investigate the effect of grid resolution on the predicted noise and acoustic parameters: Case A, a low-resolution grid [20] with $\Delta z^+ = 75$, $\Delta y^+ < 1.2$, Case B, a medium resolution grid with $\Delta z^+ = 50$, $\Delta y^+ < 1$, Case C, a high resolution grid with $\Delta z^+ = 25$, $\Delta y^+ < 1$. The span-wise and stream-wise surface grid sizes are set to be equal ($\Delta x = \Delta z$) so that the acoustic sources will be consistently resolved across the surface of the airfoil[13]. The summary of the grids' parameters is presented in Table 1.

2.2. Large-eddy simulation (LES)

Separation of the flow scales in the current LES simulation is accomplished by applying a low-pass spatial filter to the Navier-Stokes equations:

$$\frac{\partial \overline{u}_i}{\partial x_i} = 0 \tag{1}$$

$$\frac{\partial \overline{u}_i}{\partial t} + \frac{\partial \overline{u}_i \overline{u}_j}{\partial x_j} = -\frac{1}{\rho}\frac{\partial \overline{p}}{\partial x_i} + \nu \frac{\partial^2 \overline{u}_i}{\partial x_j \partial x_j} - \frac{\partial \tau_{ij}}{\partial x_j} \tag{2}$$

In which $\overline{u}_i$ and $\overline{p}$ represent the filtered velocity and pressure respectively, and τ_{ij} is the subgrid-scale (SGS) stress tensor which appears as the result of the filtering process and is defined as

$$\tau_{ij} = \overline{u_i u_j} - \overline{u}_i \overline{u}_j \tag{3}$$

To close the above system of governing equations, modeling the SGS stress tensor is needed. Applying the Boussinesq hypothesis [21] the trace-free form of SGS stress tensor is proportional to the mean resolved strain rate tensor through the following relation

$$\tau_{ij}^* = \tau_{ij} - \frac{1}{3}\tau_{kk}\delta_{ij} = -2\nu_{sgs}\overline{S}_{ij} \tag{4}$$

in which δ_{ij} is the Kronecker delta, ν_{sgs} is the

SGS eddy viscosity and $\bar{S}_{ij}$ is the filtered strain rate tensor defined as

$$\bar{S}_{ij} \equiv \left(\frac{\partial \bar{u}_i}{\partial x_j} + \frac{\partial \bar{u}_j}{\partial x_i} \right) / 2 \tag{5}$$

Based on the Smagorinsky SGS stress model [22] SGS eddy viscosity can be evaluated as

$$\nu_{sgs} = C_S \bar{\Delta}^2 \left| \bar{S} \right|, \tag{6}$$

where $\bar{\Delta}$ is the grid-level filter width, and $\left| \bar{S} \right| \equiv \sqrt{2\bar{S}_{ij}\bar{S}_{ij}}$ is the norm of $\bar{S}_{ij}$ and C_S is the model constant. Smagorinsky's model has a constant which is not universal and needs calibration.

Germano et al. [23] and subsequently Lilly [24] developed a procedure in which the Smagorinsky model constant, C_S, is dynamically computed based on the information provided by the resolved scales of motion. In this model, a test-grid-level filter is introduced with the size twice the size of the grid level filter such that $\tilde{\Delta} = 2\bar{\Delta}$.

In Dynamic Smagorinsky Model (DSM) the SGS stress tensor is calculated as

$$\tau_{ij}^{*} \overset{\text{def}}{=} \tau_{ij} - \frac{\tau_{kk}}{3}\delta_{ij} = -2C_s \bar{\Delta}^2 \left| \bar{S} \right| \bar{S}_{ij}, \tag{7}$$

Where the dynamic model coefficient C_S can be obtained from

$$C_s = -\frac{M_{ij} \mathrm{L}_{ij}^{*}}{M_{mn} M_{mn}} \tag{8}$$

Where L_{ij} is the resolved Leonard type stress defined as $\mathrm{L}_{ij} \overset{\text{def}}{=} \bar{u}_i \bar{u}_j - \bar{u}_i \bar{u}_j$, and $M_{ij} \overset{\text{def}}{=} 2\tilde{\Delta}^2 \left| \tilde{\bar{S}} \right| \tilde{\bar{S}}_{ij} - 2\bar{\Delta}^2 \left| \bar{S} \right| \bar{S}_{ij}$ is the difference between test grid and grid level base tensors.

The C_S computed by DSM varies in time and space over a wide range. To avoid numerical instability C_S is clipped between 0.1 and 0.23 by default[25].

2.3. Acoustic modeling

Lighthill's aeroacoustic analogy [7, 26] also known as the acoustic analogy is derived by rearranging governing Navier-Stokes equations of fluid flow. The result is an inhomogeneous wave equation:

$$\frac{1}{a_0^2}\frac{\partial^2 p'}{\partial t^2} - \nabla^2 p' = \frac{\partial^2 T_{ij}}{\partial x_i \partial x_j} \tag{9}$$

In which p' is the sound pressure in the far-field$\left(p' = p - p_0 \right)$, a_0 is the speed of sound, ρ_0 is the freestream density and T_{ij} is defined as the Lighthill stress tensor. The right-hand side of the equation represents the source term while the left-hand side terms show the spatial and temporal propagation of sound. The source term contains all types of sources as it is derived directly from the Navier-Stokes equations. The far-field sound pressure level can then be found by volume integrals over the domains containing sound sources. The main limitation of Lighthill's equation is that it is restricted to the unbounded fluid. Therefore, its application is limited to problems like jet noise where solid surfaces do not play a major role[27].

Ffowcs Williams et al. [8] included the influence of arbitrary moving surfaces. In this method, the fluid is partitioned into two different regions by a mathematical surface $(f = 0)$ which surrounded the sound sources. Similar to Lighthill's analogy, continuity and Navier-Stokes equations are manipulated to arrive at an inhomogeneous wave equation as follows

$$\begin{aligned} \frac{1}{a_0^2}\frac{\partial^2 p'}{\partial t^2} - \nabla^2 p' &= \frac{\partial^2}{\partial x_i \partial x_j}\left\{ T_{ij} H(f) \right\} \\ &- \frac{\partial}{\partial x_i}\left\{ \left[P_{ij} n_j + \rho u_i \left(u_n - v_n \right) \right] \delta(f) \right\} \\ &+ \frac{\partial}{\partial t}\left\{ \left[\rho_0 v_n + \rho \left(u_n - v_n \right) \right] \delta(f) \right\} \end{aligned} \tag{10}$$

Where u_i, v_i and n_i are fluid velocity, surface velocity, and the unit vector in x_i −direction respectively, and u_n, v_n are fluid velocity and surface velocity components normal to the surface. $\delta(f)$ and $H(f)$ are the Dirac delta function and Heaviside function respectively.

T_{ij} is the Lighthill stress tensor defined as

$$T_{ij} = \rho u_i u_j + P_{ij} - a_0^2 \left(\rho - \rho_0 \right) \delta_{ij} \tag{11}$$

P_{ij} is the compressive stress tensor. For a Stokesian fluid is given by

$$P_{ij} = p\delta_{ij} - \mu \left[\frac{\partial u_i}{\partial x_j} + \frac{\partial u_j}{\partial x_i} - \frac{2}{3}\frac{\partial u_k}{\partial x_k}\delta_{ij} \right] \tag{12}$$

The wave equation can be integrated analytically under the assumptions of the free-space flow and the absence of obstacles between the sound sources and the receivers. The complete solution consists of surface integrals and volume integrals. The surface integrals represent the contributions from monopole and dipole acoustic sources and partially from quadrupole sources, whereas the volume integrals represent quadrupole sources in the region outside the source surface. The contribution of the volume integrals becomes small when the flow is low subsonic, and the source surface encloses the source region. In this research, the volume integrals are dropped. Thus, we have

$$p'(\vec{x},t) = p_T'(\vec{x},t) + p_L'(\vec{x},t) \tag{13}$$

Where

$$4\pi p_T'(\vec{x},t) = \int_{f=0}\left[\frac{\rho_0(U_n+U_r)}{r(1-M_r)^2}\right]dS + \int_{f=0}\left[\frac{\rho_0 U_n\{rM_r + a_r(M_r-M^2)\}}{r^r(1-M_r)^3}\right]dS \tag{14}$$

$$4\pi p_L'(\vec{x},t) = \frac{1}{a_0}\int\left[\frac{\dot{L}_r}{r(1-M_r)^2}\right]dS + \int_{f=0}\left[\frac{L_r - L_M}{r^2(1-M_r)^2}\right]dS + \frac{1}{a_0}\int_{f=0}\left[\frac{L_r\{rM_r + a_d(M_r-M^2)\}}{r^2(1-M_r)^3}\right]dS \tag{15}$$

Where

$$U_i = v_i + \frac{\rho}{\rho_0}(u_i - v_i) \tag{16}$$

$$L_i = P_{ij}\hat{n}_j + \rho u_i(u_n - v_n) \tag{17}$$

The various subscripted quantities appearing in Eq. 14 and Eq. 15 are the inner products of a vector and a unit vector implied by the subscript. For instance, $L_r = \vec{L}\cdot\hat{\vec{r}} = L_i r_i$ and $U_n = \vec{U}\cdot\vec{n} = U_i n_i$, where $\vec{r}$ and $\vec{n}$ denote the unit vectors in the radiation and wall-normal directions, respectively. The Mach number vector M_i in Equation and Equation relates to the motion of the integration surface: $M_i = v_i/a_o$.

2.4. Solution method

Instead of a uniform flow as initialization for LES, a steady-state RANS solution is used. This reduces the computational costs of LES significantly and will yield a quasi-stationary state for transient flow more rapidly. The SIMPLE algorithm is used for steady-state RANS and the k-ε model is applied as the viscous model. In LES, dynamic Smagorinsky-Lilly is selected as the SGS model, and the model's constant is defined dynamically in time and space. Since in this the aerodynamic sound caused by external flow around a body will be calculated, the convective effects option is enabled. A non-iterative fractional step method is used for pressure-velocity coupling in transient LES with second-order central differencing for pressure and momentum and a Green-Gauss node-based method for the evaluation of pressure gradients.

The time step size required in LES calculations is governed by the time scale of the smallest resolved eddies. That requires the local Courant-Friedrichs-Lewy (CFL) number to be of an order of 1. As it is generally difficult to know the proper time step size at the beginning of the simulation an adjustment has been done after the flow is established. A time step size of $\Delta t = 5\times10^{-6}$ s is selected. For a given time step Δt, the highest frequency that the acoustic analysis can produce is $f = 1/(2\Delta t)$. resulting in a maximum observable frequency of 100 kHz. The flow is solved for a physical time of 0.03 s where it has passed the airfoil three times. After that, the time marching is continued for 4000 time-steps, and the acoustic data are saved.

3. Results and Discussion

3.1. Flow Analysis

The flow results are first analyzed by taking a closer look at the flow around the airfoil. The instantaneous velocity field around the airfoil is shown in Fig. 3 for the three different grid resolutions. All different grids are showing almost the same behavior of fluid flow around the airfoil. As expected, the incoming flow decelerates approaching the airfoil to its stagnation point at x/c = 0. For about $0 < x/c < 0.8$, the flow is accelerated on both sides of the airfoil and is in the presence of a favorable

pressure gradient due to the surface curvature. For x/c > 0.8, the flow becomes turbulent, and transition occurs near the trailing edge. For a more accurate determination of the transition point, the instantaneous skin friction coefficient is plotted along the airfoil surface in Fig. 4. The results show the skin friction coefficient as a smooth and stable curve decreasing up to approximately x/c = 0.75 where its value approaches zero. For x/c > 0.7, the instantaneous skin friction coefficient fluctuates substantially, providing an indication of both boundary layer separation from the airfoil surface and subsequent transition. Thus, the transition occurs at approximately x/c = 0.75 and it is in good agreement with the experimentally reported location for the transition point[28]. The skin friction prediction by Xfoil is also compared to the instantaneous skin friction data from LES.

After achieving the quasi-stationary state, the pressure coefficient distribution of the airfoil is stored for computing the mean values. Figure 5 shows the time-averaged pressure coefficient of airfoil obtained from LES, compared with the experimental results[29]. The results show a good agreement between the pressure coefficient obtained from LES and the experimental data in all three cases upstream of the transition location. A slight difference can be observed in the turbulent region x/c > 0.75 for different cases. It could be concluded that in the laminar region all the three mesh resolutions are accurate enough for calculating pressure coefficient distribution and the aerodynamic properties of the airfoil as well, whereas the grid resolution could affect the prediction of pressure coefficient distribution in the turbulent region. Since the TBL-TE noise is produced from the interaction of the turbulent boundary layer and the trailing edge the difference in predicted pressure fluctuations in the turbulent boundary layer could affect the prediction of the noise level.

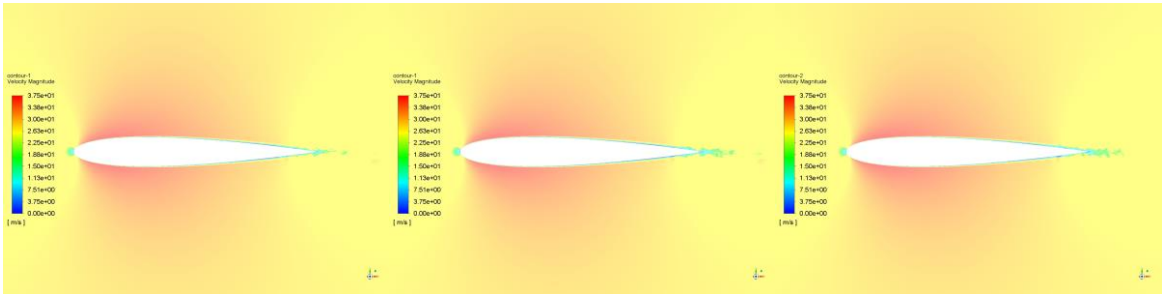

Fig. 3. Velocity magnitude at zero angle of attack from left to right grid A, B, and C

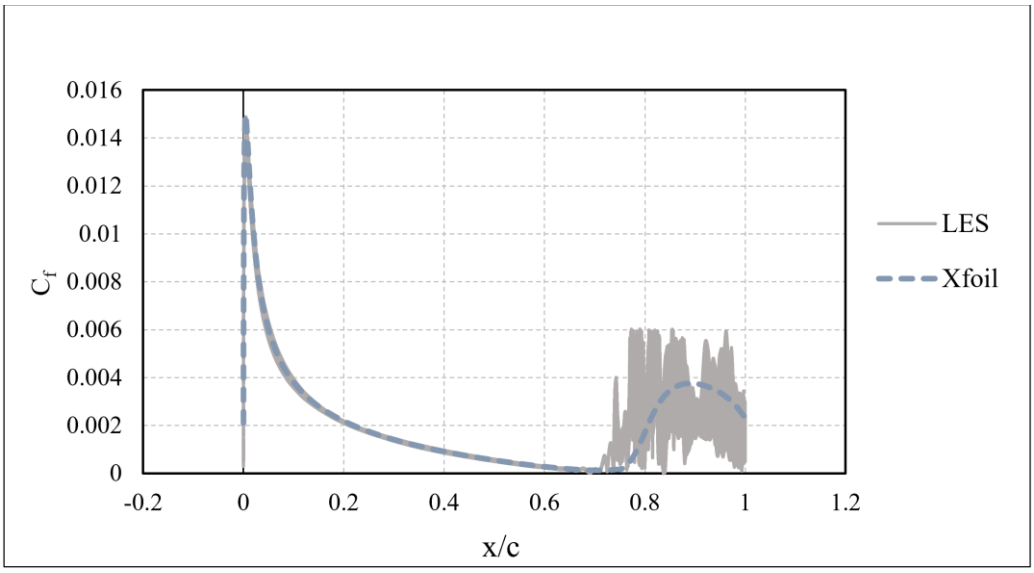

Fig. 4. Skin friction coefficient for NACA0012 at zero angle of attack, and Re = 6.4×10^5 compared with Xfoil results.

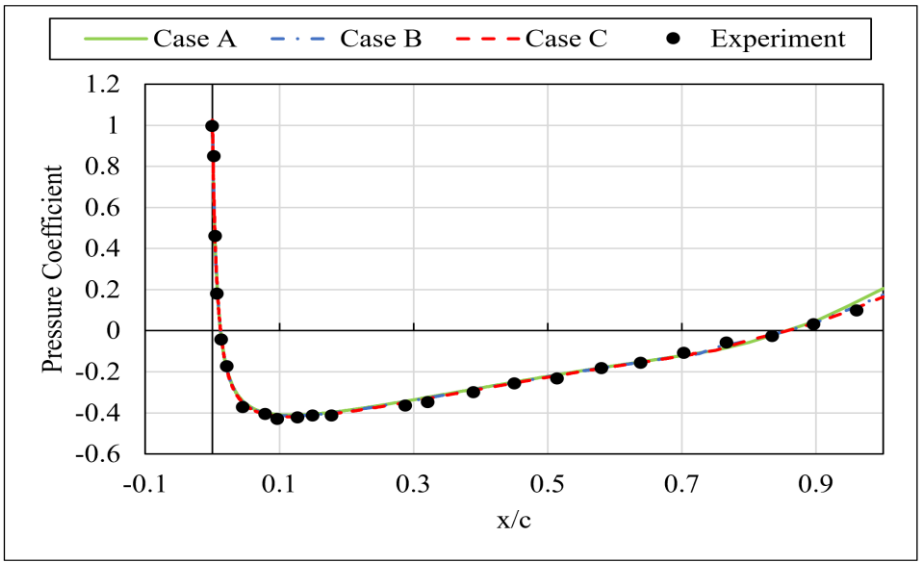

Fig. 5. Pressure Coefficient distribution of NACA0012 at zero angle of attack obtained from LES compared with experimental data [29]

3.2. Acoustic Analysis

For far-field noise measurement, a receiver is positioned perpendicular to, and 4c from the trailing edge at the model midspan. Both the experimental data[6] and predicted noise by LES and FW-H analogy are normalized to make them comparable. Scaled 1/3-octave sound pressure level spectra is achieved through the normalization proposed by Brooks et al. [6]. The sound pressure level is scaled by

$$\text{Scaled}SPL_{\frac{1}{3}} = SPL_{\frac{1}{3}} - 10\log\left(M^5 \frac{\delta_p L}{r_e^2}\right) \tag{18}$$

where M is the Mach number, L is the spanwise extent wetted by the flow, r_e is the observer distance and δ_p is the boundary layer thickness on the pressure side, which is equal on both sides at zero angle of attack. The Strouhal number based on the boundary layer thickness is defined as

$$St = \frac{f\delta_p}{U} \tag{19}$$

Figure 5 shows the scaled 1/3 octave SPL spectra for 3 different computational grids compared to the available experimental data.

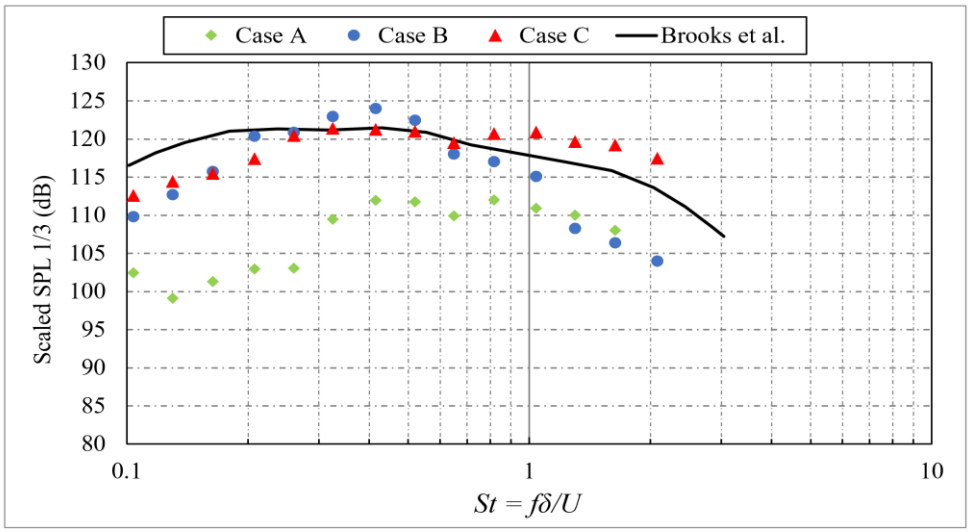

Fig. 6. Scaled 1/3 octave Sound Pressure Level spectra for NACA0012 airfoil at zero angle of attack and Re = 6.4×10^5 compared with experimental results[6]

As can be seen in Fig. 6., case A underpredicts the sound pressure level as much as 20 and 10 dB in low and high Strouhal numbers corresponding to low and high frequencies respectively, but the frequency in which SPL has its local maximum is predicted correctly to be near St = 0.4. Results of case B with higher resolution approaches the experimental noise predictions especially in the mid-range Strouhal numbers $0.2 < St < 1$ and the difference decrease to less than 10 dB in low and high Strouhal numbers. The location of the local maximum has been predicted correctly but an overprediction of less than 5 dB is observable for the magnitude of the maximum SPL. Also, an underprediction of 5-10 dB has occurred for case B at both the low and high frequencies. Looking at the results of case C, a much better agreement can be seen between the predicted noise from LES and the experimental data in almost all frequency ranges and the prediction of the frequency of maximum SPL. The differences between the noise prediction results of case C and the experimental results are less than 5 dB in low and high frequencies and less than 1 dB in the mid-range. Still, an underprediction of about 5 dB is visible in low Strouhal numbers whereas the SPL is overpredicted for less than 5 dB in high Strouhal numbers. It could be concluded that the predicted SPL of the airfoil self-noise from LES is significantly sensitive to the grid resolution adjacent to the wall surfaces. Low grid resolutions (Δz^+=75) may result in an underprediction of the SPL. This underprediction might be due to the unresolved turbulence structures of the flow and hence the wall pressure fluctuations which are the sources of the TBL-TE noise. As much as the resolution gets higher the predicted SPL approaches the experimental results and for a high-resolution grid (Δz^+=25) the predicted SPL from LES is in good agreement with experimental data, however, some over and underpredictions are still visible.

For a better comparison and quantification of sensitivity, an error is defined as the average percentage difference with the experimental measurements. The effect of grid resolution on error is shown in Fig.7. As can be seen by increasing the grid resolution from low(Δz^+=75) to high(Δz^+=25) the error is decreased significantly from 10.33% to 2.04%.

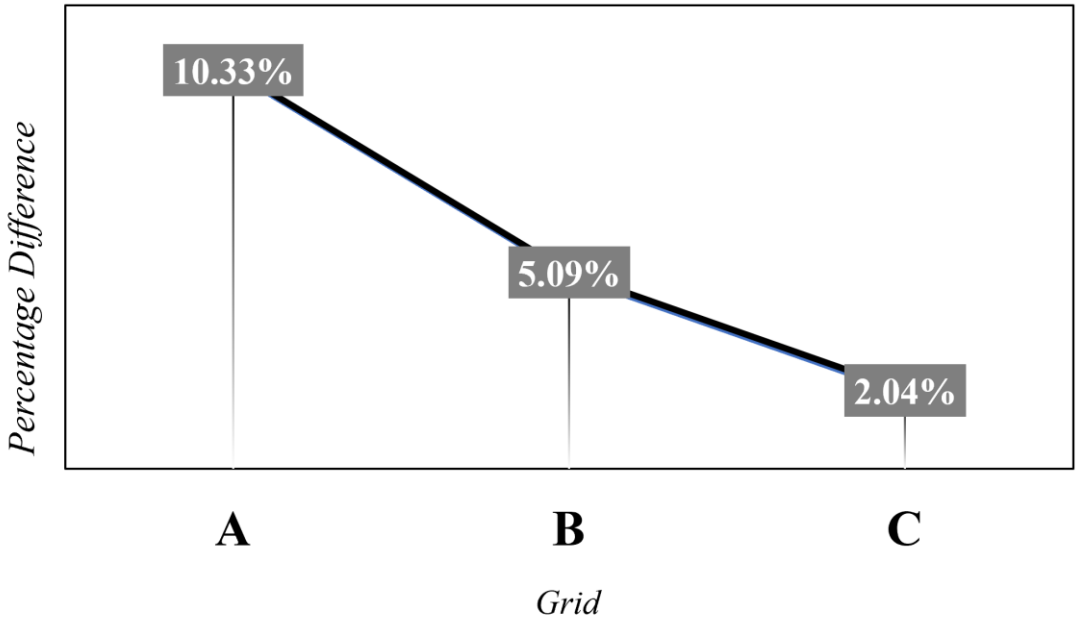

Fig. 7. Average percentage difference of scaled 1/3 octave Sound Pressure Level with experimental data for three different grid resolutions

4. Conclusion

A large-eddy simulation of three-dimensional fluid flow around a NACA0012 airfoil at zero angle of attack has been performed at Re = 6.4×10^5 on three different grid resolutions. Far-field noise has been calculated using FW-H acoustic analogy and compared with the experimental data extracted from the wind tunnel tests. The predicted noise SPL is significantly affected by grid resolution, while the effect on aerodynamic properties is negligible. The frequency at which maximum SPL occurs is almost predicted correctly by all the grids. But in the grid with low resolution (Δz^+=75), underprediction of about 10-20 dB is observed almost in all Strouhal numbers. By increasing the resolution to Δz^+=50, the difference with experimental data is reduced, especially in low and mid-range Strouhal numbers. Noise SPL obtained on the high-resolution grid (Δz^+=25) shows a good agreement in almost all Strouhal numbers with a difference of less than 5 dB with experimental data. As a quantification of the sensitivity to grid resolution, an error equal to the average percentage difference with experimental data has been calculated for each grid. It's observed that increasing the resolution by decreasing Δz^+ from 75 to 50 and 25 reduces the error from 10.33% to 5.09% and 2.04% which is a significant change.

It could be concluded that although a grid resolution is accurate enough for predicting aerodynamic properties, it could result in noise predictions with significant errors. Hence, aerodynamic parameters are less sensitive to grid resolution than the noise prediction by the FW-H method.

References

[1] Winkler, J., et al., Trailing-edge broadband noise prediction of an airfoil with boundary-layer tripping. Journal of Sound and Vibration, 2020. 482.

[2] L. Mackowski, T.H.C., Wind Turbine Trailing Edge Noise: Mitigation of Normal Amplitude Modulation by Individual Blade. Journal of Sound and Vibration, 2021. 458.

[3] Chen, W., et al., On trailing edge noise from propellers with interactions to shear layers. Journal of Sound and Vibration, 2021. 495.

[4] Jia, Z. and S. Lee, Aerodynamically induced noise of a lift-offset coaxial rotor with pitch attitude in high-speed forward flight. Journal of Sound and Vibration, 2021. 491.

[5] De Gennaro, M., et al., Semi-Empirical Modelling of Broadband Noise for Aerofoils. 2011. p. 1498-1502.

[6] Brooks, T., F, D. Pope, S, and M. Marcolini, A,, Airfoil Self-Noise and Prediction. 1989, NASA 1218.

[7] Lighthill, M.J., On sound generated aerodynamically .I. General theory. Proc. Roy. Soc. A, 1952. 211: p. 564-587.

[8] Williams, F. and D.L. Hawkins, Sound Generation by Turbulence and Surfaces in Arbitrary Motion. Philosophical Transactions of the Royal Society of London, 1969. 264(No. A 1151): p. 321-342.

[9] Lilly, G., On the Noise from Jets. AGARD CP-131, 1974: p. 13.1–13.10.

[10] Winkler, J., S. Moreau, and T. Carolus. Airfoil Trailing Edge Noise Prediction from Large-Eddy Simulation: Influence of Grid Resolution and Noise Model Formulation. in 16th AIAA/CEAS Aeroacoustics Conference. 2010.

[11] Arakawa, C., et al., Numerical approach for noise reduction of wind turbine blade tip with earth simulator. J. Earth Simul., 2005. 2(3): p. 11-33.

[12] Wang, M. and P. Moin, Computation of trailing-edge flow and noise using large-eddy simulation. AIAA Journal, 38(12), 2000: p. 2201–2209.

[13] Wasala, S., H,, et al., Aeroacoustic noise prediction for wind turbines using Large Eddy Simulation. J. Wind Eng. Ind. Aerodyn. 145, 2015: p. 17-29.

[14] Winkler. Large-Eddy Simulation and Trailing-Edge Noise Prediction of an Airfoil with Boundary-Layer Tripping. in 15th AIAA/CEAS Aeroacoustics Conference. 2009.

[15] Wolf, W.R. and S.K. Lele, Trailing-Edge Noise Predictions Using Compressible Large-Eddy Simulation and Acoustic Analogy. AIAA Journal, 2012. 50(11): p. 2423-2434.

[16] Chen, N., et al., Effects and mechanisms of LES and DDES method on airfoil self-noise prediction at low to moderate Reynolds numbers. AIP Advances, 2021. 11(2).
[17] David P. Lockard, M.M.C.a.P.G.B., Grid Sensitivity Study for Slat Noise Simulations, in 20th AIAA/CEAS Aeroacoustics Conference. 2014 Atlanta, GA.
[18] Ueno, Y. and A. Ochi, Airframe Noise Prediction Using Navier-Stokes Code with Cartesian and Boundary-fitted Layer Meshes, in 25th AIAA/CEAS Aeroacoustics Conference. 2019.
[19] Yin, Y., Y. Shi, and W. Song, Mesh Study for Airfoil Trailing Edge Noise Predictions Using RANS CFD, in Aiaa Aviation 2020 Forum. 2020.
[20] Breuer, M., Boundary Conditions for LES, in Large-Eddy Simulation for Acoustics. 2007, Cambrifge University Press. p. 201–215.
[21] Hinze, J.O., Turbulence. 1975, New York: McGraw-Hill Publishing Co.
[22] Smagorinsky, J., General Circulation Experiments with the Primitive Equations. Monthly Weather Review, 1963: p. 99-164.
[23] Germano, M., et al., A dynamic subgrid-scale eddy viscosity model. Phys. Fluids A: Fluid Dyn., 1989-1993: p. 1760-1765.
[24] Lilly, D.K., A Proposed Modification of the Germano Subgrid-Scale Closure Model. Physics of Fluids, 1992. 4: p. 633-635.
[25] ANSYS, I., ANSYS Fluent Theory Guide. Canonsburg.
[26] Lighthill, M.J., Sound generated aerodynamically. II. Turbulence as a source of sound. Proc. Roy. Soc. A, 1954. 222: p. 1-32.
[27] Lighthill, M.J., Jet Noise. AGARD Report, 1963: p. 448.
[28] Kianoosh, Y. and A. Razeghi. Determination of the Critical Reynolds Number for Flow over Symmetric NACA Airfoils. in AIAA Aerospace Sciences Meeting. 2018. Kissimmee, Florida.
[29] Gregory, N. and C. O'Reilly, L,, Low-Speed Aerodynamic Characteristics of NACA0012 Aerofoil Section, Including the Effects of Upper-Surface Roughness Simulating Hoar Frost. 1970, Aeronautical Research Council Reports and Memoranda.